Research Article

# High energy facets and oxygen vacancies guided hierarchical tin dioxide microcubes assembled by cross-stacked nanoslices for ethanol gas-sensing

Minchen Hou [a,b,1], Xianwang Deng [a,1], Shaopeng Wang [a,c], Hao Fu [d,e], Kefu Yu [a,c], Liwei Wang [a,c,*], Xiyong Chen [e,*], Shaolong Zhang [b,**]

[a] School of Marine Sciences, Coral Reef Research Center of China, Guangxi Laboratory on the Study of Coral Reefs in the South China Sea, Guangxi University, Nanning 530004, China
[b] College of Chemistry and Environmental Engineering, Shenzhen University, Shenzhen 518060, China
[c] Southern Marine Science and Engineering Guangdong Laboratory (Zhuhai), Zhuhai 519080, China
[d] School of Chemistry and Chemical Engineering, Guangxi University, Nanning 530004, China
[e] School of Resources, Environment and Materials, Guangxi University, Nanning 530004, China

## ARTICLE INFO

## ABSTRACT

For metal oxide gas sensors, the upstream theoretical mechanism can provide both quantum guidance for screening favorable materials and important insights in fabricating electronic devices. However, except for widely popular Yamazoe's 'receptor-transducer-utility' model, some specific theoretical models still lack for diverse sensing properties of metal oxide semiconductor currently. Based on a deeper understanding of surface catalytic mechanism, n-type SnO$_2$ was selected as an example to screen a better solution. Herein, hierarchical SnO$_2$ microcubes assembled from cross-stacked nanoslices were synthesized via a self-templated method, and the SnO$_2$ microcubes displayed versatile performances with excellent response to 100 ppm ethanol (Sr = Rair/Rgas = 56.9), relative low optimal working temperature of 170 °C, good repeatability under high R.H. (90%) and ultra-low detection limit even under 0.1 ppm. The performances of SnO$_2$ nanofilms, hierarchical SnO$_2$ nanotubes and commercial SnO$_2$ powder were also studied. The results showed that the increase of exposed higher energy facet of (101) and rich oxygen vacancies on 3D-crossed nanoslices of SnO$_2$ microcubes contribute to outstanding gas sensing performances, which were also confirmed by the DFT calculations. These demonstrate a diverse sensing mechanism and a new insights for state-in-art gas sensing materials of SnO$_2$.

© 2022 Elsevier B.V. All rights reserved.

## 1. Introduction

Sensor is a functional device for sensing, collecting, converting, transmitting and processing all kinds of information. It is one of the important infrastructures for modern science and technology, particularly gas sensors exhibit extraordinary performance in toxic/explosive gas detection, indoor and outdoor pollutant monitoring, environmental quality evaluation, exhaled gas diagnosis and breath analysis. During the past several years, considerable efforts have been continuously devoted to exploring the design and synthesis of sensing materials with various dimensional and morphological structures from nanostructured individuals or their heterojunctions [1–5]. Among these, metal oxide semiconductor (MOS)-based gas sensors have evoked strong ardor due to their highly stability, easy fabrication, low cost and device compatibility [6–8]. Typically, the n-type SnO$_2$-based gas sensors have been widely researched [9–13] and various nanostructured SnO$_2$ hosts exhibit quite different gas-sensing properties in selectivity, sensitivity, limit of detection, and so on [14,15], indicating the gas sensing properties are significantly affected by the construction mode. With the tremendous contribution to developing SnO$_2$-based gas sensors, theoretical mechanism can be as driving force of the quantum guidance for screening
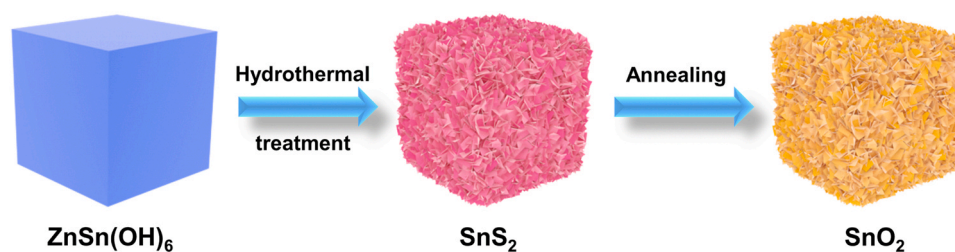
---

**Fig. 1.** Illustration of the synthetic process of hierarchical $SnO_2$ microcubes.

favorable gas sensing materials and important insights in fabricating electronic devices. However, some specific explanations or theoretical quantum models, including the widely accepted Yamazoe's 'receptor-transducer-utility' model which is based on the transfer of electrons between surface-adsorbed oxygen and conduction band [10,11,16,17], are still insufficient to elucidate how structural changes affect the gas sensitivity. What's more, it is rarely reported on how to control the design of high-performance $SnO_2$-based gas-sensitive nanomaterials in theory to date [18–20], and thus screening of high performance $SnO_2$-based sensing-materials is impeded to some extent. In consequence, it remains a great challenge to select a proper mechanism to give in-depth understanding of the structural design for $SnO_2$-based gas-sensitive nanomaterials.

To the best of our knowledge, the gas sensitive mechanism of n-type metal oxides semiconductor such as $SnO_2$ sensor materials depends on the surface reactions between the oxygen vacancies behaving a filled donor state and gas molecules. Oxygen molecules in the air occupying the oxygen vacancies and then capturing electrons from the materials result in forming negative oxygen species. Once the reducing gas enters, it will react with negative oxygen species on the surface of the sensitive material and release electrons. As a result, the resistance changes of the sensitive material give rise to the sensing response. Hence, the enhancement of oxygen vacancies concentrations to obtain more active sites would play a crucial part on the sensing performance to the target gas. Thereinto, Zhang et al. [10] reported that the enhanced gas sensing performance of $SnO_2$ can be achieved through engineering crystal structures with controllable exposure of specific high energy facets. The facets of (110) and (101) are often exposed in $SnO_2$, while the surface energy of (101) is relatively higher than that of (110). Hence, obtaining $SnO_2$ nanomaterials with more exposed (101) crystal planes is beneficial to improve gas sensitivity [10,21]. Furthermore, the effect of other synthesis-process-dependent structural parameters (morphology, grain size, surface defect, etc.) on sensing performances can't be ignored as well [22], since the sensing properties can be enhanced with larger specific surface area and abundant oxygen defects [23–25]. In addition, the experimental characterizations and theoretical calculations make a tremendous contribution to get the clarification of comprehensive sensing nature [26–32], as well as the development of nanoscaled devices with flexible and wearable features [21,33].

Herein, we elaborately designed an efficient modified self-templated strategy to fabricate 3D n-type $SnO_2$ microcubes, which were assembled from cross-stacked nanoslices as well as containing rich oxygen defects. The 3D n-type $SnO_2$ microcubes was achieved by initially fabricating hierarchical $SnS_2$ microboxes precursor via hydrothermal treatment of $ZnSn(OH)_6$ cubes. Then, gradually heating and annealing transformed the $SnS_2$ precursor into randomly cross-assembled nanoslices with thicknesses of 10–15 nm. The prepared $SnO_2$ microcubes dominates higher energy facet (101), which provide more active sites for gas adsorption and finally enhance the gas sensitivity. Besides, the 3D n-type $SnO_2$ microcubes behave the

highest oxygen vacancy $(O_V)$, which can afford more active oxygen species to participate in the oxidation-reduction reaction occurring on the surface of catalytic materials. Compared to $SnO_2$ nanofilms, hierarchical $SnO_2$ nanotubes and commercial $SnO_2$ powder, the prepared $SnO_2$ microcubes possess excellent sensing response to ethanol with incomparable gas selectivity. Meanwhile, the $SnO_2$ microcubes exhibited high response magnitude, relative low optimal operating temperature, good repeatability under high R.H. (Relative Humidity) and acceptable response/recovery times, as well as low detection limit. Moreover, density functional theory (DFT) calculations revealed that the relatively higher adsorption energy facet of (101) and the involvement of $O_V$ on the building nanoslices of hierarchically cubic structure play an irreplaceable role on surface-molecule adsorption ability for ethanol. This study would provide new insights and guidance in preparing remarkable functional materials in gas sensing.

## 2. Experimental section

### 2.1. Synthesis of hierarchical $SnO_2$ microcubes

The multistep production of the hierarchical $SnO_2$ microcubes is illustrated in Fig. 1. Firstly, hydroxide $ZnSn(OH)_6$ cubes were prepared by a co-precipitation method. Secondly, after hydrothermal treatment, the $ZnSn(OH)_6$ cubes transformed into $SnS_2$, namely in situ phase transition of the obtained $ZnSn(OH)_6$ cubes precursor without changing the spatial layout. Lastly, since $SnS_2$ is easy to be oxidized at a high temperature, the $SnO_2$ microcubes product was obtained by annealing the $SnS_2$ microboxes under the air atmosphere.

### 2.2. Synthesis of $ZnSn(OH)_6$ cubes

A modified co-precipitation method was utilized to prepare $ZnSn(OH)_6$ cubes [34]. Specifically, 10 mL of absolute ethanol containing $SnCl_4\cdot5H_2O$ (0.701 g) was added into 70 mL of $ZnCl_2$ (0.273 g) and citric acid (0.384 g) aqueous solution under stirring. Then, 10 mL of NaOH (2 M) solution was added drop by drop into the above solution and kept stirring for 1 h. Additional 30 mL of NaOH (2 M) solution was later added again for further 30 min reaction. The white $ZnSn(OH)_6$ precipitate was harvested by centrifugation, washed with DI water and absolute ethanol, and dried at 60 °C in vacuum.

### 2.3. Synthesis of hierarchical $SnS_2$ microboxes

The $SnS_2$ microboxes assembled by hierarchically stacked nanoflakes can be synthesized via the self-template method [35]. Typically, 0.572 g of $ZnSn(OH)_6$ template, 0.160 g of $H_4EDTA$ and 0.090 g of TAA were dispersed into 40 mL of DI water, and then transferred into a 100 mL of Teflon-lined autoclave and maintained at 220 °C for 3 h. When cooled down, the yellow $SnS_2$ products were rinsed by
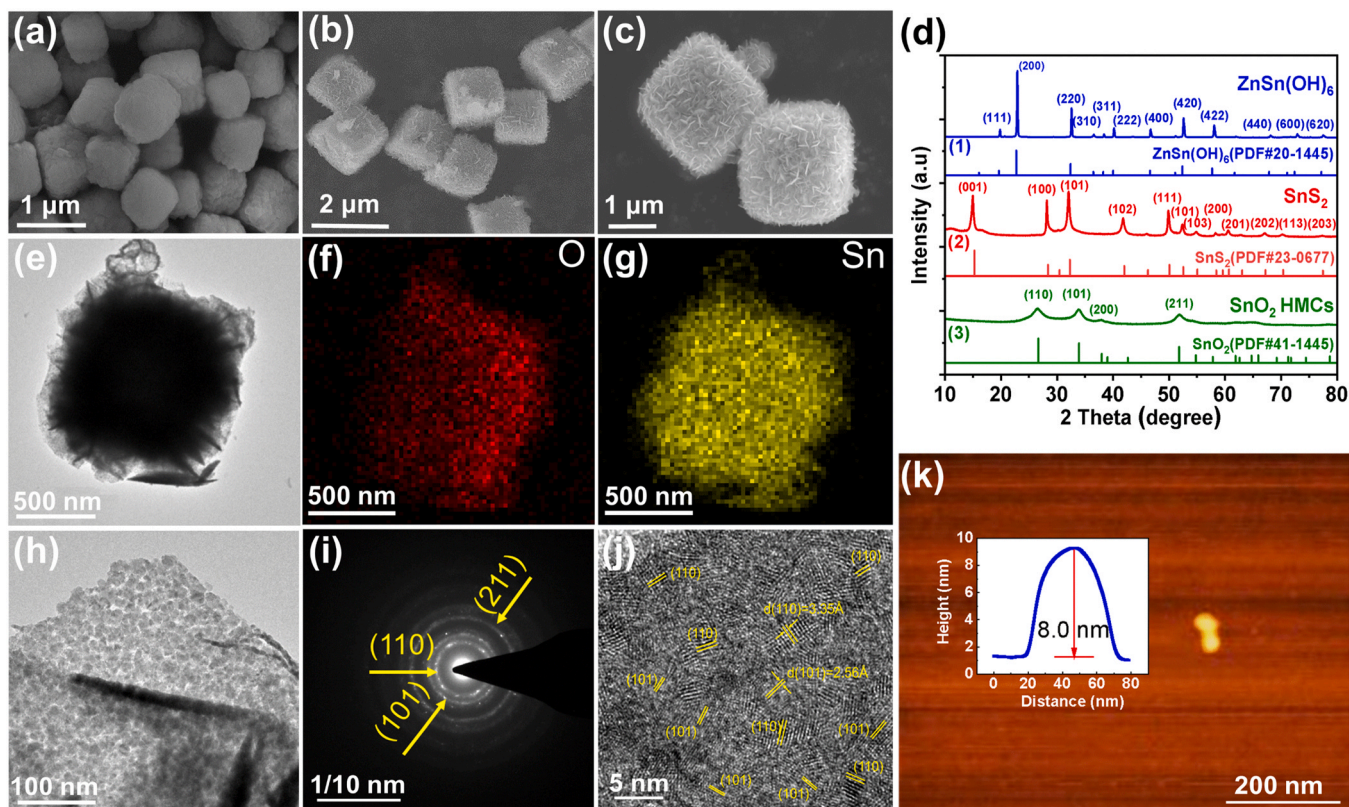
**Fig. 2.** (a–c) SEM images of ZnSn(OH)$_6$ cubes, SnS$_2$ microboxes, and hierarchical SnO$_2$ microcubes (S1); (d) XRD patterns corresponding to (a–c); (e) TEM image and (f–g) EDX elemental mapping of S1; (h) HRTEM image of nanoslice in S1; (i) The corresponding SAED pattern; (j) HRTEM image with lattice fringe; (k) AFM image and the surface height variation curve of nanoslice in S1.

absolute ethanol several times and dried at 60 °C to get the SnS$_2$ microboxes.

### 2.4. Synthesis of hierarchical SnO$_2$ microcubes

Hierarchical SnO$_2$ microcubes (labeled as Sample 1, S1) were in situ transformed from the self-templated synthesized hierarchical SnS$_2$ microboxes precursor. The SnS$_2$ precipitate was annealed in the air by the following procedures to obtain SnO$_2$ microcubes: the precursor was heated to 400 °C at a heating rate of 2 °C/min with intermittent 20 min temperature holdings at 200 °C and 300 °C, then finally kept annealing at 400 °C for 5 h.

For comparison, SnO$_2$ nanofilms (labeled as Sample 2, S2) and hierarchical SnO$_2$ nanotubes (labeled as Sample 3, S3) were prepared. More details can be seen in the Supporting Information (SI). Besides, commercial SnO$_2$ powder (labeled as Sample 4, S4) was also used as a contrast.

### 2.5. Material characterizations

The structure, morphology, specific area, as well as the chemical state of SnO$_2$ samples were characterized by means of powder X-ray diffraction (XRD, Rigaku Ultima IV, Japan; Cu Kα radiation, λ = 1.5418 Å), field emission scanning electron microscope (FESEM, SU5000, Japan), transmission electron microscopy (TEM), selected-area electron diffraction (SAED), and high-resolution TEM (HRTEM, FEI Tecnai G2 f20 s-twin, 200 KV, USA) with energy dispersive X-ray detector (EDX), N$_2$ adsorption-desorption isotherms based on the Brunauer-Emmett-Teller (BET) equation (ASAP 2020, Micromeritics, USA), X-ray photoelectron spectroscopy (XPS, Thermo Scientific

Escalab 250Xi, Al Ka X-ray monochromator), atomic force microscope (AFM, Hitachi 5100 N) and electron spin resonance (ESR, JES-FA300, Japan).

### 2.6. Gas sensor assembly and sensing test

Gas-sensing tests were performed on a CGS-8 intelligent static test system (Beijing Elite Tech Co. Ltd., China) (Fig. S1), enabling precise control of the gas flow, the gas composition, and the measurement of electrical resistance. During the whole process, dry air was used as the reference and gas balance. Besides, certain water vapor was pre-mixed with ethanol vapor and air at room temperature (20 °C) to reach tunable R.H., and the sensor response is defined as $S = R_a/R_g$ for reductive gases, where $R_a$ is the sensor resistance in air, and $R_g$ is the sensor resistance in target gas phase [36]. The details have been described in our previous works [36,37], more details can be also found in the SI.

### 2.7. Computational methods

DFT (density functional theory) calculations were carried out using Vienna Ab-initio Simulation Package (VASP) for all the geometry structures in this work [38]. The exchange-correlation interactions of the molecules and surface were described by the generalized gradient approximation (GGA) with the Perdew-Burke-Ernzerhof (PBE) function [39,40]. The cut-off energy was set at 400 eV for the plane-wave basis set, and the convergence criterion for the energy and force was set to 10$^{-5}$ eV and 0.02 eV/Å, respectively. The vacuum space was set of 15 Å in the z-direction. A

Monkhorst-Pack $2 \times 2 \times 1$ k-point grid was adopted to sample the Brillouin zone. The DFT-D3 method was adopted in this work [41].

The adsorption energy ($E_{ad}$) for various molecule adsorption schemes on surface were calculated and using the following Eq. (1):

$$E_{ad} = E_{surface} + E_{molecule} - E_{surface-molecule} \tag{1}$$

where $E_{surface-molecule}$, $E_{surface}$ and $E_{molecule}$ are the energies for the molecule adsorption on the surface, the clean surface and isolated molecule, respectively.

## 3. Results and discussion

### 3.1. Material characterizations

The morphologies of $ZnSn(OH)_6$ cubes, $SnS_2$ microboxes and $SnO_2$ microcubes were observed using SEM. Fig. 2a shows that uniform $ZnSn(OH)_6$ cubes with slightly flat surface, exhibiting regular configurations with an edge length of about 1.0–1.2 μm and no ill-shaped impurities on the smooth surfaces. In Fig. 2b, the $SnS_2$ intermediate displays the hierarchical cubic structure with a large amount of nanoslices and a few thick undifferentiated films, conversely the edge length is up to ~ 1.4 μm due to volume expansion after in situ reaction. The hierarchical microcubes structures can be clearly disclosed by the SEM (Fig. 2c), which are randomly cross-assembled by sharp nanoslice with thicknesses of 10–15 nm. Additionally, the corresponding phase transitions from $ZnSn(OH)_6$ to $SnO_2$ can be precisely reflected by XRD test, as shown in Fig. 2d. The diffraction pattern of the initial precursor gives consistent peaks with $ZnSn(OH)_6$ phase (JCPDS No. 20–1455) [42,43], and all the sharp peaks in the pattern indicate its high crystallization. The average crystallite size of the intermediate $SnS_2$ phase (JCPDS No. 23–0677) [36] is estimated as 20.2 nm using Scherrer formula based on (001) facet of the XRD data, while the broadened diffraction patterns of tetragonal rutile $SnO_2$ phase (JCPDS No. 41–1445) reveal the average crystallite size of ~ 7.5 nm based on (110) facet. The broader peak of $SnO_2$ may come from the increasing fine nano-crystals generated from thermal decomposition of highly crystallized $SnS_2$ precursor. The increased disordered degree from ultra-thin nanoslices units constructed hierarchically in various directions may also contribute to such diffraction peak broadening. Such thin nanounits, as well as the smaller grain size of ~ 7.5 nm, match well with overwhelming acknowledgement that sensor response can increase drastically when the crystallite sizes drop below about $2\lambda_D$ (Debye length, often several nanometers) [10,16,17].

The TEM image in Fig. 2e shows that the hierarchical S1 is composed of various crossly-dispersed ultrathin nano-petals. The EDX patterns in Fig. 2f and g prove the uniform distribution of O and Sn elements in the microcubes. In particular, the HRTEM and SAED images in Fig. 2h and i reveal that plenty of nanoparticles comprise the polycrystalline nanoslices with porous texture. Besides, the significant (110), (211) and (101) crystal planes in Fig. 2i are consistent with the above mentioned XRD results. The clear lattice fringes with spacing of 0.335 and 0.256 nm are indexed to the (110) and (101) crystal planes of S1 [36,44], according to the HRTEM image in Fig. 2j. It is worth noting that the facet energy of (101) is higher than that of the more stable (110) facet [10,16,36], and the enhancement of sensitivity and selectivity benefits from the increase of (101) crystal plane which can accelerate the adsorption of target gas component. Besides, the thickness of nanoslices is obtained at approximate 8 nm from AFM test, as shown in Fig. 2k. Meanwhile, the morphologies of S2-S4 have also been assessed via SEM presented in Fig. S2. As can be seen, the micro-structures of the samples are nanofilms, hierarchical nanotubes and amorphous small particles, respectively.

In order to detect the influence of microscopic construction on the surface permeability, the specific surface area and pore size distribution of S1-S4 were measured by $N_2$ adsorption-desorption isotherms. As shown in Fig. 3a–d, all the curves exhibit a typical IV curve with a H3 hysteresis loop. The surface areas of S1-S4 are determined by the BET to be about 101.2, 94.4, 45.5 and 9.4 $m^2 \ g^{-1}$, respectively. The highest surface area of S1 may be attributed to the hierarchical microcubes structure which is constructed by numbers of cross-stacked nanoslices. Meanwhile, the corresponding BJH pore size distributions present the mesopores structure with diameters centered at 6.2, 3.4 and 5.0, 3.4 and 17.5, 3–10 nm for S1, S2, S3 and S4, respectively. Overall, the highest surface area and relatively moderate pore channels for S1 can be beneficial to efficient adsorption and transfer of gas molecules.

According to the Gibbs-Wulff theorem in crystallography [45], the tetragonal rutile structure is the most stable/equilibrium form of $SnO_2$ at atmospheric pressure with one Sn atom coordinated by six O atoms, and (110) with the lowest energy facet dominates the natural crystal surface. However, the crystal facets with higher energy are usually more active than those lower ones, resulting in a better gas sensing performances due to high density of atomic steps and edges as well as dangling bonds [46]. As is reported, the surface densities of dangling bonds for (110) and (101) facets of $SnO_2$ are about 14.0559 $nm^{-2}$ and 14.7917 $nm^{-2}$, respectively, which means the facet energy of (101) is higher than that of (110) [47]. Therefore, the appearance and increase of (101) facet are beneficial to the improvement of gas sensitivity for $SnO_2$. As shown in Fig. 4a, all the XRD patterns of S1-S4 belong to the rutile phase (JCPDS No. 41–1445), while the peak intensities corresponding to the same diffraction angle varies obviously. The height ratios of (101) to (110) reflections in S1-S4, denoted as $H_{(101)/(110)}$, are calculated as 0.95, 0.88, 0.73 and 0.77, respectively (Fig. 4b). It further proved that the higher energy facet (101) dominates in S1, which thus would greatly boost the gas sensitivity of S1 [48–50].

In addition, XPS was applied to compare the elemental chemical valence and binding energy of the samples. The full XPS survey and Sn 3d spectra for S1-S4 are presented in Fig. S3a–b, showing the absence of impurities. The O 1s peaks for all the samples can be fitted into two peaks, as shown in Fig. 4c. The reconvolution of O 1 s spectra reveals two different chemical states of oxygen species: lattice oxygen ($O_L$) indexed to Sn-O bonds, and oxygen vacancy ($O_V$) on the surface [51]. The $O_V$ plays an essential role as active sites for chemi-adsorption of oxygen molecules and further reaction on the surface of sensing materials [47,52]. Therefore, the increment of $O_V$ content means that more active oxygen species can participate in the oxidation-reduction reaction occurring on the surface of catalytic materials, and give rise to a larger enhancement in sensor response. The $O_V$ contents of as-prepared samples are considerably dissimilar. The derived ratios of $O_V/O_L$ for S1-S4 are 1.33, 0.59, 0.40 and 0.23, respectively (Fig. 4b). Amazingly, rarely reports showed $O_V$ content higher than $O_L$ in $SnO_2$ nanomaterials. The abundance of $O_V$ content on the surface of the sample can also be identified with ESR characterization (Fig. 4d). A strong and conspicuous peak at g= 2.0027 is indexed to the electrons trapped in oxygen vacancies [53]. What' s more, the highest intensity peak displayed in S1, which is consistent with the conclusions from XPS characterization. Benefiting from the hierarchically cubic configuration built by cross-stacked nanoslices, S1 owns high active surfaces and numerous diffusion channels to accelerate the gas molecule adsorption-desorption and mass transfer process, due to the increase of high energy crystal plane and abundant oxygen defects. Hence, the favorable raised gas sensing performances of S1 can be expected.

To clarify the discrepancy in the sensing performance on various facets, the atomic stacking models of (110) and (101) facets are
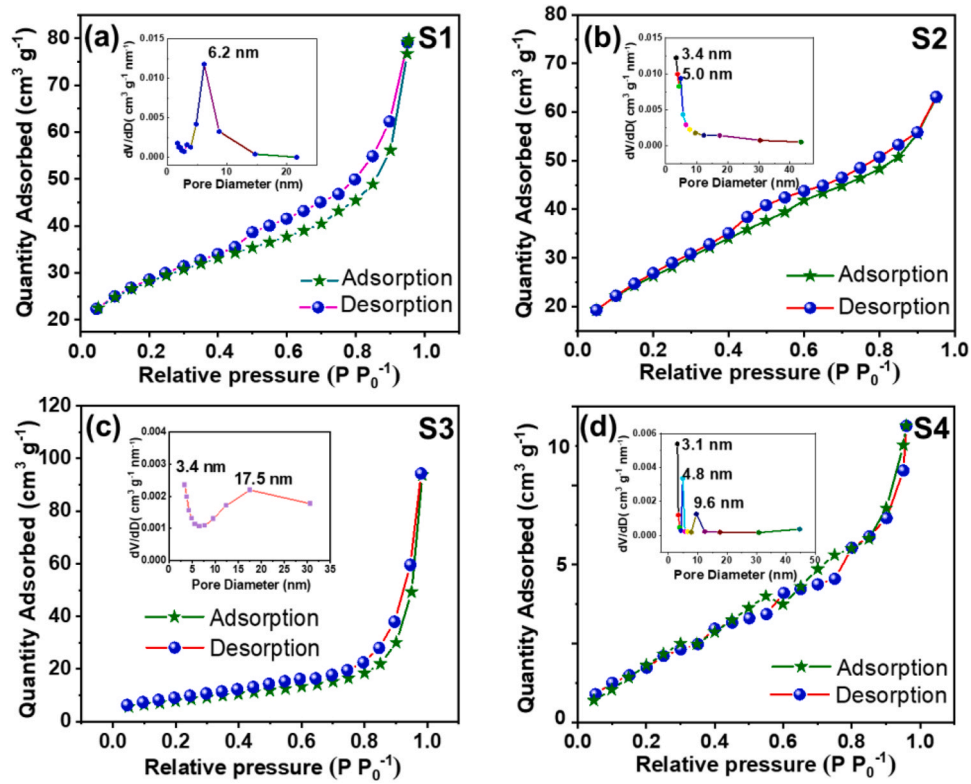
**Fig. 3.** (a–d) $N_2$ adsorption-desorption isotherms of S1-S4, respectively. Inset images are the corresponding pore size distribution plots of S1–S4, respectively.
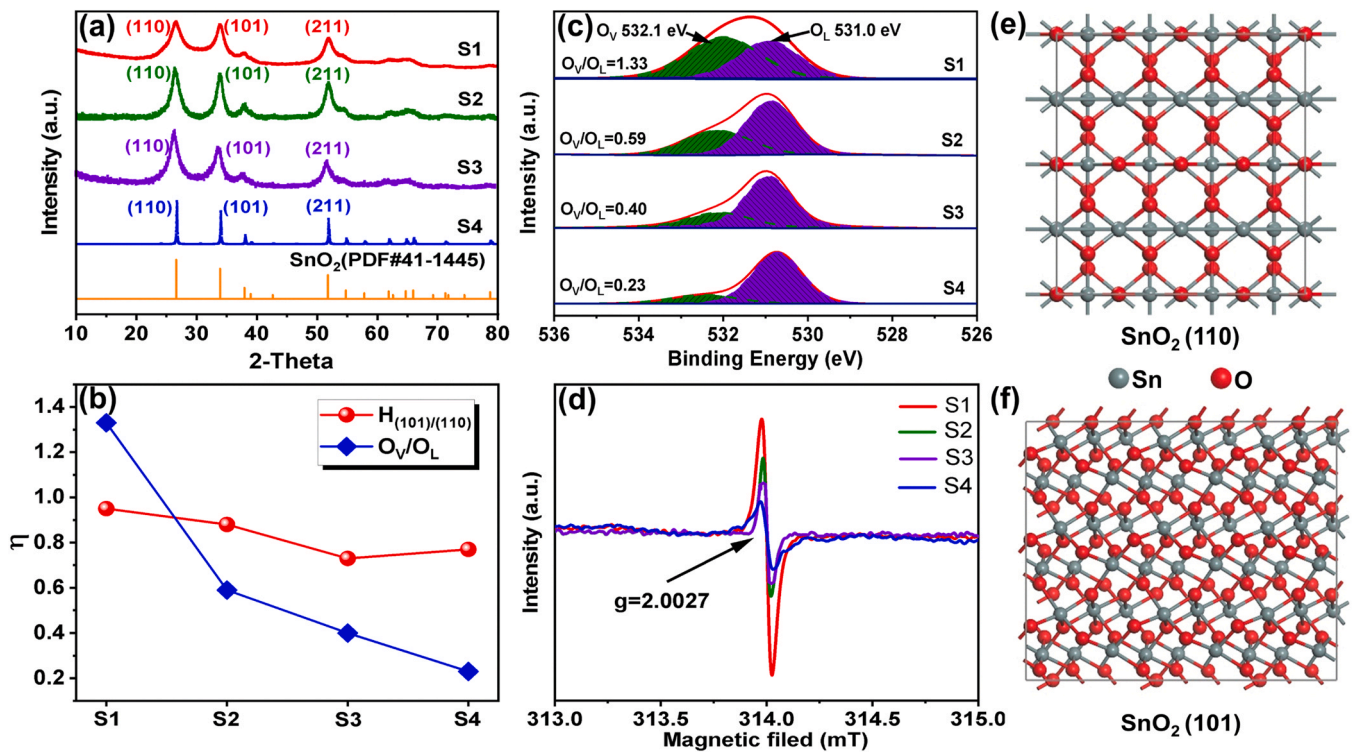


**Fig. 4.** (a) XRD patterns of S1–S4; (b) Coefficients associated with the height ratios of (101)/(110) and integral area ratios of $O_V/O_L$; (c) High-resolution O 1s spectra from XPS data of S1–S4; (d) The ESR spectrum of S1–S4; (e and f) Atomic stacking model of (110) and (101) crystal planes for $SnO_2$.
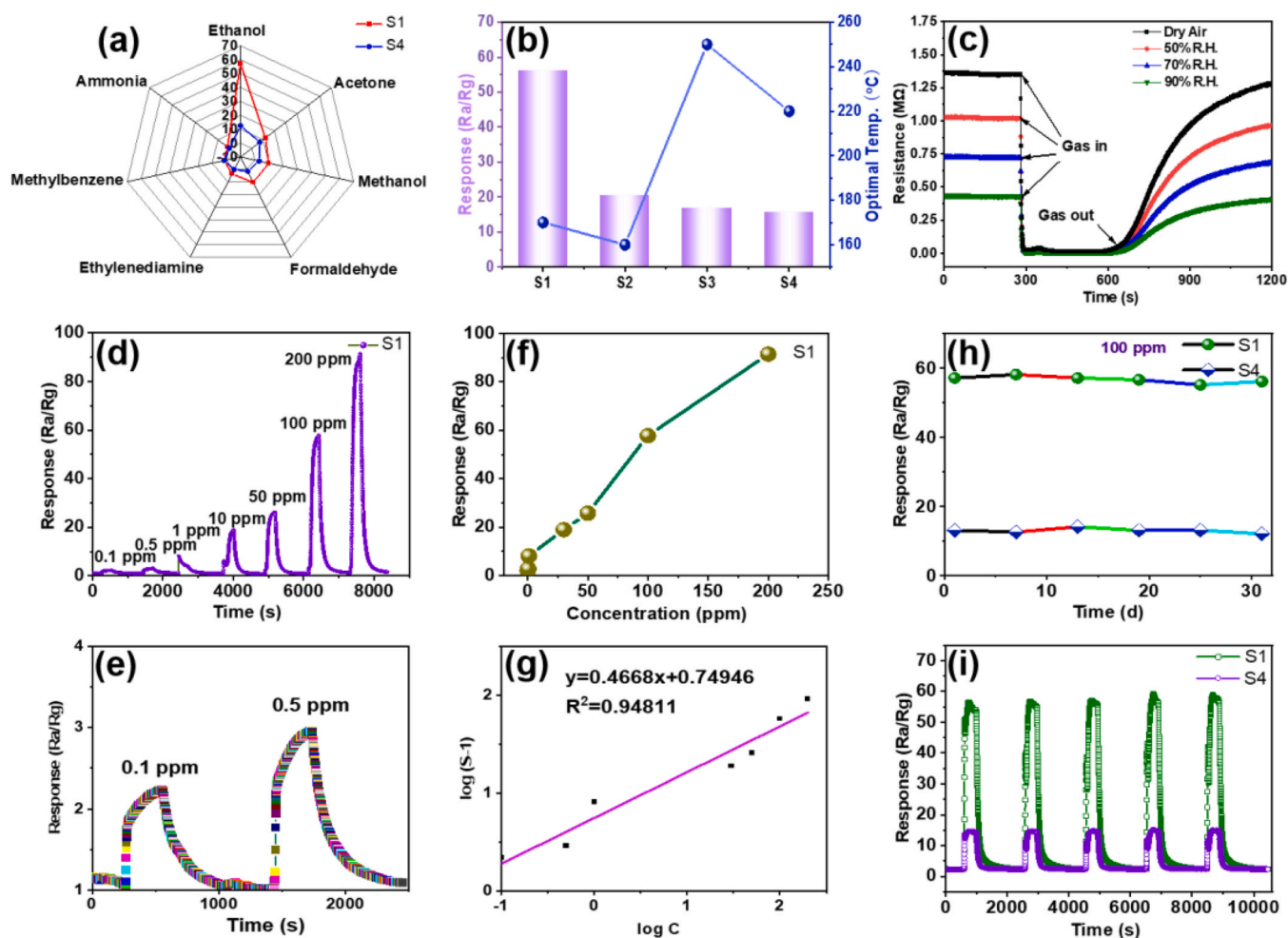
**Fig. 5.** (a) Selectivity of S1 and S4 to 100 ppm of different gas components (ethanol, acetone, methanol, formaldehyde, ethylenediamine, methylbenzene and ammonia) at 170 °C in dry air; (b) Comparison of the optimal operating temperature and the corresponding response to 100 ppm ethanol for S1-S4 in dry air; (c) The effect of various R.H. values on dynamic resistance transient of S1 at 170 °C; (d–e) Dynamic response transients of the S1-based sensor to ethanol from 0.1 to 200 ppm; (f–g) The corresponding dependence of the response signal on the ethanol concentration; (h) Long-term response stability curves of S1 and S4-based sensors to 100 ppm ethanol within 30 days; (i) Response reproducibility of S1 and S4-based sensors to 100 ppm ethanol. All the tests were carried out in dry air at 170 °C.

established in Fig. 4e and f to exhibit the density of dangling bonds on each surface [10,36]. The (110) facet is terminated with both O and Sn atoms, while (101) facet is almost O⁻ atoms terminated. The difference of the atomic density among the two facets implies higher content of oxygen defects in crystal plane with more O⁻ terminated dangling bonds [10,47].

### 3.2. Gas sensing performances

As well known, excellent selectivity towards the target gas is still the main goal of metal oxide-based sensors. Hence, the selectivity property of SnO₂-based sensor to different gas components (ethanol, acetone, methanol, formaldehyde, ethylenediamine, methylbenzene and ammonia) was investigated in this study. Operating temperature is always an important character for gas sensors and the optimal working temperature for S1 was 170 °C (Fig. S4a). The corresponding gas sensing response concerning a fixed concentration of 100 ppm of each component in dry air and at 170 °C is shown in Fig. 5a. S1-based sensor exhibits the highest response to ethanol (denoted as Sr = 56.9), which is about over five times more than that of acetone, methanol and formaldehyde, and it is insensitive to the amines and aromatic hydrocarbons. Comparatively, the responses of S4

counterpart are much lower and the sensor even doesn't respond to most gases. Meanwhile, the associated adsorption calculations by DFT simulation to explain the selectivity can be seen in the following discussion.

For the comparisons of the highest responses to 100 ppm ethanol, the corresponding optimal operating temperature (OOT) of S1-S4 were shown in Fig. 5b. Obviously, the sensor based on S1 gives the highest response of 56.9 to ethanol at quite low temperature of 170 °C, which is much lower than commonly reported temperature (≥ 200 °C) [10,11,16]. As comparisons, the OOT for S2-S4 are 160, 250 and 220 °C with ethanol responses as 20, 17.5 and 15, respectively. In addition, the OOT of S1 is also lower than those used in quite a lot studies listed in Table S1. The phenomenon may be ascribed to the interaction between target gas component and the plentiful exposed higher energy facet of (101) with the emergence of oxygen vacancies. The resistance of MOS-based gas sensor can be significantly affected by temperature, as is shown in Fig. S4b. When the operating temperature increases, more electron hole pairs of S1 will be produced accompanying with enriching the density of carriers, leading to the decline of actual baseline resistance.

Moreover, the response of fabricated gas device tends to decrease from the dry air to humid atmosphere, i.e., with an increase of the
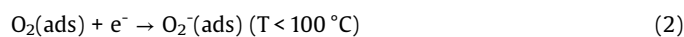
relative humidity (R.H.). Therefore, R.H. is one of the key parameters in evaluating the sensing characteristics during the process of measurement and application. The effect of various R.H. (0, 50%, 70% and 90% in air) on dynamic resistance transient of S1 at 170 °C with 100 ppm ethanol was investigated and the results were presented in Fig. 5c. Along with the increase of R.H. values, the basic resistance significantly decreases from about 1.35 down to 0.43 MΩ, and the resistance descending amplitude also diminishes with the injection of ethanol gas, consistent with the corresponding dynamic response changes in Fig. S5, the response value exhibits a trend of gradual reduction with increase of R.H. in the gas phase. Such adverse effect of R.H. on sensing properties have been discussed in our previous work due to the inevitable chemi-sorption/physi-sorption of $H_2O$ molecules which replace partial $O^{\delta-}$ species pre-adsorbed on the sensor surface, thus part of occupied electrons will return from $O^{\delta-}$ to the conduction band of $SnO_2$, reducing the basic resistance of the conductive material [36]. Regardless of this, the response in Fig. S5 still keeps high enough even at higher R.H. in the gas phase, i.e., above 18.8 when the R.H. is up to 70%, and about 9.6 at R.H. of 90%. Surprisingly, the response-recovery times are not affected evidently even though in the environment with high humidity. This to some extent indirectly demonstrates the preferential-adsorption ability of ethanol molecules using S1 as the sensing material. Consequently, the result proves the excellent ethanol preference of S1 than other counterparts, and the stable maintenance to ethanol sensing even in high humidity conditions.

What's more, the dynamic response transient curves to ethanol in the range of 0.1–200 ppm can be seen in Fig. 5d and e (the corresponding actual resistance transient plot is shown in Fig. S6a), which demonstrates an acceptable response/recovery rate for S1-based sensor, i.e., the response/recovery time is within ~13 s and ~68 s, respectively. Besides, the response value of S1-based device to ethanol presents a linear increasing tendency from 0.1 to 200 ppm, and the highest response value of 92–200 ppm ethanol is achieved, as shown in Fig. 5f. Although the response to the much lower ethanol concentration in air won't follow the general linear tendency, it still presents a reasonable meaningful response as seen in Fig. 5g. The dependence of response value on ethanol concentration with the sensors aforementioned can be expressed by $S = a[C]^b + 1$ [54], where S is the sensor response value, C represents the concentration of the target ethanol. At a certain operating temperature, the above equation can be rewritten as $\log(S-1) = b \log(C) + \log(a)$, demonstrating the linear relationship between S and C in a logarithm format. Therefore, the limit of detection using S1 sensing material can be below 0.1 ppm even as low as dozens of ppb, which is typically superior than those conventional counterparts. A long-time stability evaluation of S1 sensor in a successive 30-day period (Fig. 5h) is also carried out to demonstrate its highly stable and durable sensing performance to 100 ppm ethanol in dry air at 170 °C. The response value of S1-based sensor remains almost constant in the range of 56–58 with very slight deviations. Practically, the successful application of a sensing material in a sensor relies not only on its sensitivity but also on its response reproducibility. As illustrated in Fig. 5i, S1 exhibits an excellent repeatable response during the 5 cycles. In order to present a more realistic resistance change trend of S1-based sensor, the actual resistance change corresponding to Fig. 5i has been given in Fig. S6b, where the basic resistance value in air remains at around 1.35 MΩ. These results indicate the excellent stability properties of the S1-based sensor device to ethanol. What's more, the ethanol sensing properties of S1 is comparable to those obtained by others reported $SnO_2$-based nanomaterials (Table S1), indicating its advantages of an excellent ethanol gas-sensing performance.

### 3.3. Sensing mechanism

Up to now, pure $SnO_2$ has been verified as active sensing materials for detecting different gases, such as $H_2$, formaldehyde, ethanol, isopropanol and CO [55–58]. However, the mechanism of gas selectivity is still ambiguous, which somehow impedes the development of efficient sensors with ultrahigh sensing performances. In this work, the density functional theory (DFT) calculations were adopted as well to reveal the mechanism of gas selectivity of the most stable (110) and (101) lattice planes in $SnO_2$. Here, the target molecules of ethanol, formaldehyde, acetone, methanol, ethylene-diamine, methylbenzene and ammonia have been considered. The calculations revealed obviously different adsorption energies on the $SnO_2$ (110) or $SnO_2$ (101) surface for these target gas molecules. Among them, adsorption of ethanol on $SnO_2$ (101) has the highest positive adsorption energy of 1.78 eV, as shown in Fig. 6a. The adsorption energies of other gas molecules are in a descending order as follows: formaldehyde (1.44 eV), methanol (1.26 eV), ethylenedia-mine (1.21 eV), acetone (0.85 eV), ammonia (0.24 eV), and methyl-benzene (0.21 eV). The order is almost in line with the gas selectivity experiment results (Fig. 5a), suggesting the lattice face of (101) in $SnO_2$ has the highest selectivity for ethanol. Meanwhile, adsorption of ethanol on the surface of $SnO_2$ (110) has a relatively much lower adsorption energy of 0.49 eV compared to the adsorption on $SnO_2$ (101), meaning adsorption of ethanol on $SnO_2$ (110) is not encouraged at this point.

Further, the computational results revealed that the charge density difference of ethanol adsorption on $SnO_2$ (101) surface is with a maximum charge transfer of 0.5 |e| than that on $SnO_2$ (110) surface (0.17 |e|), suggesting the stronger adsorption energy of ethanol adsorption on $SnO_2$ (101) surface, as shown in Fig. 6b. Note that lots of oxygen vacancies ($O_V$) have been identified in the $SnO_2$ samples used in this work, the effects of $O_V$ on the adsorption ability of the target gas shall not be excluded. In fact, our calculations obtained the modest formation energies of $O_V$ around 1.86 eV and 1.81 eV on the surfaces of $SnO_2$ (110) and $SnO_2$ (101) correspondingly, which is in favor of $O_V$ formation on these surfaces (Fig. 6c). While introducing one Ov on the surface of $SnO_2$ (110), the ethanol adsorption energy is increased by 0.8 eV (from 0.5 eV to 1.3 eV). On the other hand, the ethanol adsorption energy is decreased by 0.3 eV from pure $SnO_2$ (101) (~1.8 eV) to defect $SnO_2$ (101) (~1.5 eV). Obviously, the ethanol adsorption energy on the defect $SnO_2$ (101) is stronger than that on defect $SnO_2$ (110), the former is more beneficial to design practical ethanol gas selectivity. In all, these experimental and theoretical results demonstrate that introduction of $O_V$ defect on $SnO_2$ surfaces could generally enhance the overall ethanol gas selectivity. Thus, it is worth noting that the key to possess the ultrahigh ethanol gas selectivity is to synthesize (101) and (110) lattice facets of $SnO_2$ with $O_V$. The specific processes are shown in Eqs. (1)–(4). The morphology of oxygen ions is related to temperature. When the working temperature is 170 °C, the main morphology of oxygen ions is $O^-$. Once exposed to ethanol gas, the preadsorbed ionized oxygen species (dominant $O^-(ads)$ at 170 °C) on $SnO_2$ surface reacts with ethanol to form $CO_2$ and $H_2O$, thus resulting in changing the surface resistance of the gas sensing material. And the specific process is shown in Eq. (5).
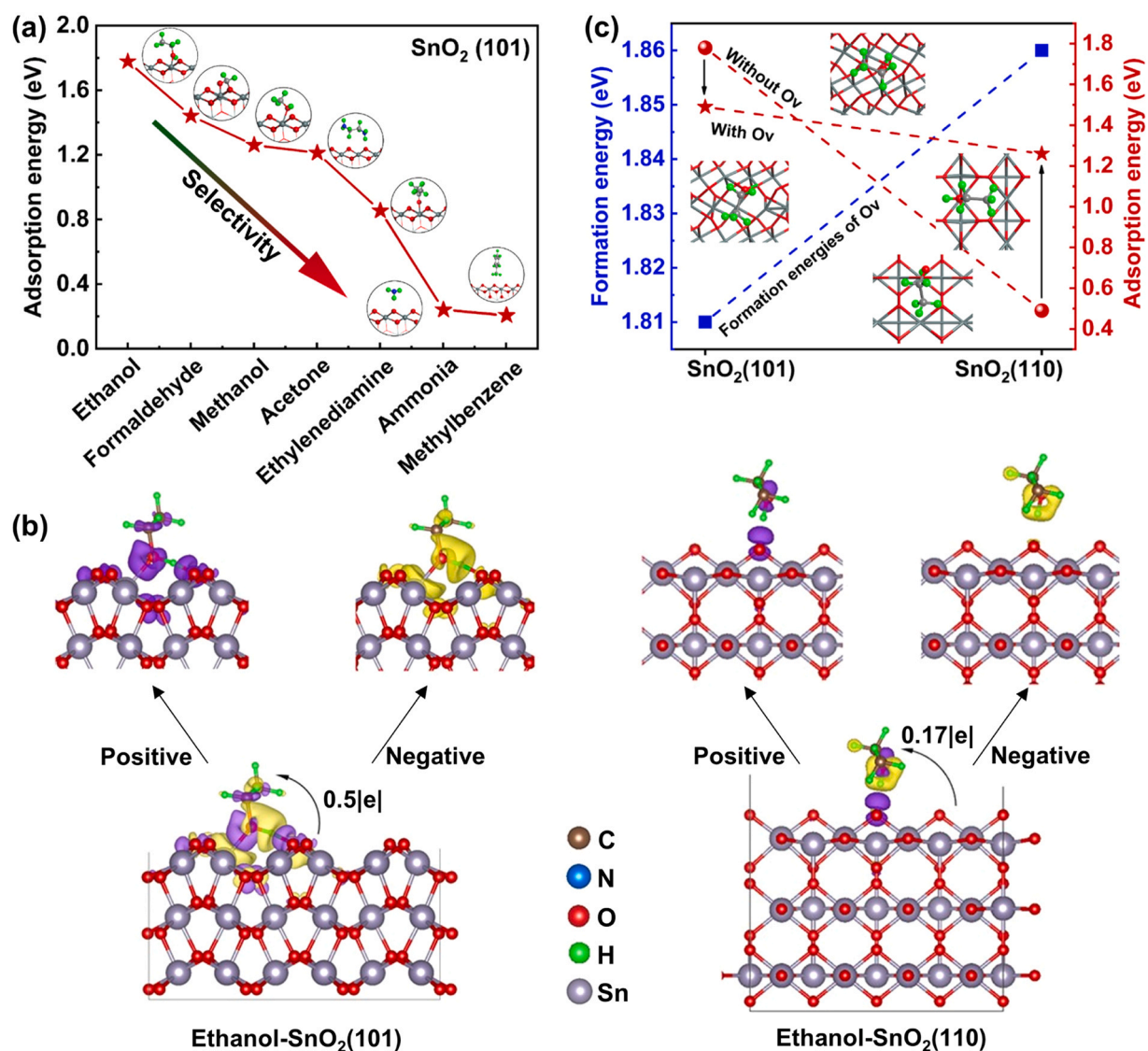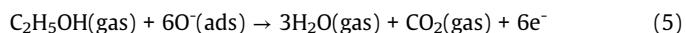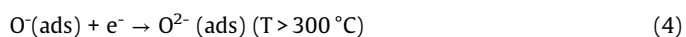
$$O_2(gas) \rightarrow O_2(ads) \tag{1}$$

$$O_2(ads) + e^- \rightarrow O_2^-(ads) \ (T < 100 \,°C) \tag{2}$$

$$O_2^-(ads) + e^- \rightarrow 2O^-(ads) \ (100 \,°C < T < 300 \,°C) \tag{3}$$

**Fig. 6.** (a) Target gas selectivity on the $SnO_2$ (101) surface; (b) Charge density difference of target gas adsorption on the $SnO_2$ (101) and $SnO_2$ (110) surfaces; (c) $SnO_2$ (101) and $SnO_2$ (110) surfaces with or without $O_V$ for ethanol gas adsorption. Note: the purple and yellow isosurfaces represent the electron accumulation and depletion (isosurface value: 0.002 e/Å$^2$).

$$O^-(ads) + e^- \rightarrow O^{2-}(ads) \ (T > 300\ °C) \tag{4}$$

$$C_2H_5OH(gas) + 6O^-(ads) \rightarrow 3H_2O(gas) + CO_2(gas) + 6e^- \tag{5}$$

## 4. Conclusions

In summary, in order to develop a novel $SnO_2$ nanostructure to improve gas sensing performances, and provide certain specific theoretical mechanism on the diverse sensing, we started the research from the n-type pure $SnO_2$. Herein, we synthesized a 3D hierarchical $SnO_2$ microcubes via a modified self-templated method, and the prepared $SnO_2$ exhibited more inimitable performances than other counterparts with favorable ethanol selectivity ($S_r$ = 56.9), good repeatability even at R.H. of 90%, relative lower optimal working temperature of 170 °C than those used in most commonly reports (≥ 200 °C), and ultra-low detection limit even under 0.1 ppm. Material characterization combined with DFT calculation implied the gas-sensing enhancing mechanism, which attributed to the increase of relatively higher energy facet of (101) and regulation of $O_V$ on the building nanoslices of hierarchically cubic structure. Ultimately, the

new insights can provide not only the quantum guidance for boosting gas sensing, but also important guidance in fabricating high performance electronic sensing devices.

**CRediT authorship contribution statement**

**Minchen Hou:** Investigation, Methodology, Writing – original draft, Writing – review & editing. **Xianwang Deng:** Conceptualization, Methodology, Writing – original draft. **Shaopeng Wang:** Formal analysis, Writing – review & editing. **Hao Fu:** Formal analysis, Writing – review & editing. **Kefu Yu:** Visualization, Writing – review & editing. **Liwei Wang:** Supervision, Writing – review & editing. **Xiyong Chen:** Supervision, Writing – review & editing. **Shaolong Zhang:** Visualization, Writing – review & editing, Supervision.

**Competing financial interests**

The authors declare no competing financial interests.

**Appendix A. Supporting information**

Supplementary data associated with this article can be found in the online version at doi:10.1016/j.jallcom.2022.164973.

## References

[1] N. Hou, Q. Sun, J. Yang, S. You, Y. Cheng, Q. Xu, W. Li, S. Xing, L. Zhang, J. Zhu, Q. Yang, Fabrication of oxygen-doped MoSe$_2$ hierarchical nanosheets for highly sensitive and selective detection of trace trimethylamine at room temperature in air, Nano Res. 13 (2020) 1704–1712.

[2] Y. Sun, J. Wang, H. Du, X. Li, C. Wang, T. Hou, Formaldehyde gas sensors based on SnO$_2$/ZSM-5 zeolite composite nanofibers, J. Alloy. Compd. 868 (2021) 159140.

[3] C. Hou, G. Tai, Y. Liu, X. Liu, Borophene gas sensor, Nano Res. 15 (2022) 2537–2544.

[4] X. Liu, X. Duan, C. Zhang, P. Hou, X. Xu, Improvement toluene detection of gas sensors based on flower-like porous indium oxide nanosheets, J. Alloy. Compd. 897 (2022) 163222.

[5] X. Liu, T. Ma, N. Pinna, J. Zhang, Two-dimensional nanostructured materials for gas sensing, Adv. Funct. Mater. 27 (2017) 1702168.

[6] M. Zhang, Y. Tang, X. Tian, H. Wang, J. Wang, Q. Zhang, Magnetron co-sputtering optimized aluminum-doped zinc oxide (AZO) film for high-response formaldehyde sensing, J. Alloy. Compd. 880 (2021) 160510.

[7] C. Lou, G. Lei, X. Liu, J. Xie, Z. Li, W. Zheng, N. Goel, M. Kumar, J. Zhang, Design and optimization strategies of metal oxide semiconductor nanostructures for advanced formaldehyde sensors, Coord. Chem. Rev. 452 (2022) 214280.

[8] S. Das, S. Mojumder, D. Saha, M. Pal, Influence of major parameters on the sensing mechanism of semiconductor metal oxide based chemiresistive gas sensors: a review focused on personalized healthcare, Sens. Actuators B Chem. 352 (2022) 131066.

[9] G. Li, Y. Fan, Q. Hu, D. Zhang, Z. Ma, Z. Cheng, X. Wang, J. Xu, Morphology and size effect of Pd nanocrystals on formaldehyde and hydrogen sensing performance of SnO$_2$ based gas sensor, J. Alloy. Compd. (2022) 163765.

[10] X. Gao, T. Zhang, An overview: Facet-dependent metal oxide semiconductor gas sensors, Sens. Actuators B Chem. 277 (2018) 604–633.

[11] Z. Song, Z. Wei, B. Wang, Z. Luo, S. Xu, W. Zhang, H. Yu, M. Li, Z. Huang, J. Zang, F. Yi, H. Liu, Sensitive room-temperature H$_2$S gas sensors employing SnO$_2$ quantum wire/reduced graphene oxide nanocomposites, Chem. Mater. 28 (2016) 1205–1212.

[12] H. Mousavi, Y. Mortazavi, A.A. Khodadadi, M.H. Saberi, S. Alirezaei, Enormous enhancement of Pt/SnO$_2$ sensors response and selectivity by their reduction, to CO in automotive exhaust gas pollutants including CO, NO$_x$ and C$_3$H$_8$, Appl. Surf. Sci. 546 (2021) 149120.

[13] N. Tammanoon, A. Wisitsoraat, A. Tuantranont, C. Liewhiran, Flame-made Zn-substituted SnO$_2$ nanoparticulate compound for ultra-sensitive formic acid gas sensing, J. Alloy. Compd. 871 (2021) 159547.

[14] S. Lu, Y. Zhang, J. Liu, H.-Y. Li, Z. Hu, X. Luo, N. Gao, B. Zhang, J. Jiang, A. Zhong, J. Luo, H. Liu, Sensitive H$_2$ gas sensors based on SnO$_2$ nanowires, Sens. Actuators B Chem. 345 (2021) 130334.

[15] D. Degler, B. Junker, F. Allmendinger, U. Weimar, N. Barsan, Investigations on the temperature-dependent interaction of water vapor with tin dioxide and its implications on gas sensing, ACS Sens. 5 (2020) 3207–3216.

[16] D.R. Miller, S.A. Akbar, P.A. Morris, Nanoscale metal oxide-based heterojunctions for gas sensing: a review, Sens. Actuators B Chem. 204 (2014) 250–272.

[17] H.-J. Kim, J.-H. Lee, Highly sensitive and selective gas sensors using p-type oxide semiconductors: overview, Sens. Actuators B Chem. 192 (2014) 607–627.

[18] Y. Shang, L. Guo, Facet-controlled synthetic strategy of Cu$_2$O-based crystals for catalysis and sensing, Adv. Sci. 2 (2015) 1500140.

[19] Q. Kuang, X. Wang, Z. Jiang, Z. Xie, L. Zheng, High-energy-surface engineered metal oxide micro- and nanocrystallites and their applications, Acc. Chem. Res. 47 (2014) 308–318.

[20] A. Gurlo, Nanosensors: towards morphological control of gas sensing activity. SnO$_2$, In$_2$O$_3$, ZnO and WO$_3$ case studies, Nanoscale 3 (2011) 154–165.

[21] R.A. Potyrailo, Multivariable sensors for ubiquitous monitoring of gases in the era of internet of things and industrial internet, Chem. Rev. 116 (2016) 11877–11923.

[22] J. He, X. Yan, A. Liu, R. You, F. Liu, S. Li, J. Wang, C. Wang, P. Sun, X. Yan, B. Kang, J. He, Y. Wang, G. Lu, A rapid-response room-temperature planar type gas sensor based on DPA-Ph-DBPzDCN for the sensitive detection of NH$_3$, J. Mater. Chem. A 7 (2019) 4744–4750.

[23] G. Jiménez-Cadena, J. Riu, F.X. Rius, Gas sensors based on nanostructured materials, Analyst 132 (2007) 1083–1099.

[24] N. Yamazoe, N. Miura, Environmental gas sensing, Sens. Actuators B Chem. 20 (1994) 95–102.

[25] Y.-F. Sun, S.-B. Liu, F.-L. Meng, J.-Y. Liu, Z. Jin, L.-T. Kong, J.-H. Liu, Metal oxide nanostructures and their gas sensing properties: a review, Sensors 12 (2012) 2610–2631.

[26] D. Wang, L. Tian, H. Li, K. Wan, X. Yu, P. Wang, A. Chen, X. Wang, J. Yang, Mesoporous ultrathin SnO$_2$ nanosheets in situ modified by graphene oxide for extraordinary formaldehyde detection at low temperatures, ACS Appl. Mater. Interfaces 11 (2019) 12808–12818.

[27] J. Miao, C. Chen, Y.S. Lin, Metal-oxide nanoparticles with a dopant-segregation-induced core–shell structure: gas sensing properties, J. Phys. Chem. C 122 (2018) 21322–21329.

[28] Y. Xiong, W. Lu, D. Ding, L. Zhu, X. Li, C. Ling, Q. Xue, Enhanced room temperature oxygen sensing properties of LaOCl–SnO$_2$ hollow spheres by UV light illumination, ACS Sens. 2 (2017) 679–686.

[29] V. Galstyan, A. Ponzoni, I. Kholmanov, M.M. Natile, E. Comini, S. Nematov, G. Sberveglieri, Investigation of reduced graphene oxide and a Nb-doped TiO$_2$ nanotube hybrid structure to improve the gas-sensing response and selectivity, ACS Sens. 4 (2019) 2094–2100.

[30] L. Zhang, J. Shi, Y. Huang, H. Xu, K. Xu, P.K. Chu, F. Ma, Octahedral SnO$_2$/graphene composites with enhanced gas-sensing performance at room temperature, ACS Appl. Mater. Interfaces 11 (2019) 12958–12967.

[31] J. Miao, C. Chen, L. Meng, Y.S. Lin, Self-assembled monolayer of metal oxide nanosheet and structure and gas-sensing property relationship, ACS Sens. 4 (2019) 1279–1290.

[32] Z. Wang, S. Gao, T. Fei, S. Liu, T. Zhang, Construction of ZnO/SnO$_2$ heterostructure on reduced graphene oxide for enhanced nitrogen dioxide sensitive performances at room temperature, ACS Sens. 4 (2019) 2048–2057.

[33] Z. Yin, Y. Bu, J. Ren, S. Chen, D. Zhao, Y. Zou, S. Shen, D. Yang, Triggering superior sodium ion adsorption on (2 0 0) facet of mesoporous WO$_3$ nanosheet arrays for enhanced supercapacitance, Chem. Eng. J. 345 (2018) 165–173.

[34] L. Zhang, H.B. Wu, B. Liu, X.W. Lou, Formation of porous SnO$_2$ microboxes via selective leaching for highly reversible lithium storage, Energy Environ. Sci. 7 (2014) 1013–1017.

[35] S. Wang, Y. Fang, X. Wang, X.W. Lou, Hierarchical microboxes constructed by SnS nanoplates coated with nitrogen-doped carbon for efficient sodium storage, Angew. Chem. Int. Ed. 58 (2019) 760–763.

[36] L. Wang, H. Fu, Q. Jin, H. Jin, H. Haick, S. Wang, K. Yu, S. Deng, Y. Wang, Directly transforming SnS$_2$ nanosheets to hierarchical SnO$_2$ nanotubes: Towards sensitive and selective sensing of acetone at relatively low operating temperatures, Sens. Actuators B Chem. 292 (2019) 148–155.

[37] L. Wang, Y. Kang, X. Liu, S. Zhang, W. Huang, S. Wang, ZnO nanorod gas sensor for ethanol detection, Sens. Actuators B Chem. 162 (2012) 237–243.

[38] G. Kresse, Ab initio molecular dynamics for liquid metals, J. Non Cryst. Solids 192–193 (1995) 222–229.

[39] J.P. Perdew, K. Burke, M. Ernzerhof, Generalized gradient approximation made simple, Phys. Rev. Lett. 77 (1996) 3865–3868.

[40] G. Kresse, J. Furthmüller, Efficiency of ab-initio total energy calculations for metals and semiconductors using a plane-wave basis set, Comp. Mater. Sci. 6 (1996) 15–50.

[41] S. Grimme, S. Ehrlich, L. Goerigk, Effect of the damping function in dispersion corrected density functional theory, J. Comput. Chem. 32 (2011) 1456–1465.

[42] L. Wang, J. Li, Y. Wang, K. Yu, X. Tang, Y. Zhang, S. Wang, C. Wei, Construction of 1D SnO$_2$-coated ZnO nanowire heterojunction for their improved n-butylamine sensing performances, Sci. Rep. 6 (2016) 35079.

[43] W.W. Wang, Y.J. Zhu, L.X. Yang, ZnO–SnO$_2$ hollow spheres and hierarchical nanosheets: hydrothermal preparation, formation mechanism, and photocatalytic properties, Adv. Funct. Mater. 17 (2007) 59–64.

[44] R. Xu, L.-X. Zhang, M.-W. Li, Y.-Y. Yin, J. Yin, M.-Y. Zhu, J.-J. Chen, Y. Wang, L.-J. Bie, Ultrathin SnO$_2$ nanosheets with dominant high-energy {001} facets for low temperature formaldehyde gas sensor, Sens. Actuators B Chem. 289 (2019) 186–194.

[45] A. Selloni, Anatase shows its reactive side, Nat. Mater. 7 (2008) 613–615.

[46] L. Gracia, A. Beltrán, J. Andrés, Characterization of the high-pressure structures and phase transformations in SnO$_2$. a density functional theory study, J. Phys. Chem. B 111 (2007) 6479–6485.

[47] C. Wang, D. Cai, B. Liu, H. Li, D. Wang, Y. Liu, L. Wang, Y. Wang, Q. Li, T. Wang, Ethanol-sensing performance of tin dioxide octahedral nanocrystals with exposed high-energy {111} and {332} facets, J. Mater. Chem. A 2 (2014) 10623–10628.

[48] V. Inderan, M.M. Arafat, S. Kumar, A.S.M.A. Haseeb, Z.-T. Jiang, M. Altarawneh, H.L. Lee, Study of structural properties and defects of Ni-doped SnO$_2$ nanorods as ethanol gas sensors, Nanotechnology 28 (2017) 265702.

[49] G. Qin, F. Gao, Q. Jiang, Y. Li, Y. Liu, L. Luo, K. Zhao, H. Zhao, Well-aligned Nd-doped SnO$_2$ nanorod layered arrays: preparation, characterization and enhanced alcohol-gas sensing performance, Phys. Chem. Chem. Phys. 18 (2016) 5537–5549.

[50] W. Yang, H.-J. Wang, R.-R. Liu, J.-W. Wang, C. Zhang, C. Li, D.-C. Zhong, T.-B. Lu, Tailoring crystal facets of metal–organic layers to enhance photocatalytic activity for CO$_2$ reduction, Angew. Chem. Int. Ed. 60 (2021) 409–414.

[51] Y. Tong, P. Chen, T. Zhou, K. Xu, W. Chu, C. Wu, Y. Xie, A. Bifunctional, Hybrid electrocatalyst for oxygen reduction and evolution: cobalt oxide nanoparticles

strongly coupled to B,N-decorated graphene, Angew. Chem. Int. Ed. 56 (2017) 7121–7125.

[52] M. Huang, S. Wang, H. Fu, H. Shao, Y. Wang, K. Yu, Y. Huang, Z. Jv, L. Wang, An efficient vapor-phase processing method derived mesoporous N-C@SnO$_2$-Co$_3$O$_4$ hollow nanoboxes with abundant surface oxygen vacancy for highly improved gas sensing application, J. Alloy. Compd. 863 (2021) 158341.

[53] L. Liu, P. Zhou, X. Su, Y. Liu, Y. Sun, H. Yang, H. Fu, X. Qu, S. Liu, S. Zheng, Synergistic Ni single atoms and oxygen vacancies on SnO$_2$ nanorods toward promoting SO$_2$ gas sensing, Sens. Actuators B Chem. 351 (2022) 130983.

[54] H. Fu, H. Shao, L. Wang, H. Jin, D. Xia, S. Deng, Y. Wang, Y. Chen, C. Hua, L. Liu, L. Zang, From a relatively hydrophobic and triethylamine (TEA) adsorption-selective core–shell heterostructure to a humidity-resistant and TEA highly selective sensing prototype: an alternative approach to improve the sensing characteristics of TEA sensors, ACS Sens. 5 (2020) 571–579.

[55] P.G. Choi, N. Izu, N. Shirahata, Y. Masuda, Fabrication and H$_2$-sensing properties of SnO$_2$ nanosheet gas sensors, ACS Omega 3 (2018) 14592–14596.

[56] S. Xu, Y. Xu, H. Zhao, R. Xu, Y. Lei, Sensitive gas-sensing by creating adsorption active sites: coating an SnO$_2$ layer on triangle arrays, ACS Appl. Mater. Interfaces 10 (2018) 29092–29099.

[57] Y. Zhang, L. Li, S. Ao, J. Wang, G. Li, Interfacial doping of heteroatom in porous SnO$_2$ for highly sensitive surface properties, ACS Omega 3 (2018) 6988–6997.

[58] G. Li, Y. Fan, Q. Hu, D. Zhang, Z. Ma, Z. Cheng, X. Wang, J. Xu, Morphology and size effect of Pd nanocrystals on formaldehyde and hydrogen sensing performance of SnO$_2$ based gas sensor, J. Alloy. Compd. 906 (2022) 163765.